Fully C^1-Conforming Subdivision Elements for Finite Deformation Thin-Shell Analysis

Fehmi Cirak and Michael Ortiz
Graduate Aeronautical Laboratories,
California Institute of Technology,
Pasadena, CA 91125, USA

Abstract

We have extended the subdivision shell elements of Cirak, Ortiz and Schröder [20] to the finite-deformation range. The assumed finite-deformation kinematics allows for finite membrane and thickness stretching, as well as for large deflections and bending strains. The interpolation of the undeformed and deformed surfaces of the shell is accomplished through the use of subdivision surfaces. The resulting 'subdivision elements' are strictly C^1-conforming, contain three nodes and one single quadrature point per element, and carry displacements at the nodes only. The versatility and good performance of the subdivision elements is demonstrated with the aid of a number of test cases, including the stretching of a tension strip; the inflation of a spherical shell under internal pressure; the bending and inflation of a circular plate under the action of uniform pressure; and the inflation of square and circular airbags. In particular, the airbag solutions, while exhibiting intricate folding patterns, appear to converge in certain salient features of the solution, which attests to the robustness of the method.

1 Introduction

The mechanical response of thin and moderately thick shells is most naturally described by the Kirchhoff-Love type shell theories incorporating the first and second fundamental form of the surface. As is well known, the related conforming finite element discretization requires C^1-continuous shape functions, or more precisely, shape functions belonging to the Sobolev space H^2. Unfortunately, for general unstructured meshes it is not possible to ensure C^1 continuity in the conventional sense of strict slope continuity across finite elements when the elements are endowed with purely local polynomial shape functions and the nodal degrees of freedom consist of displacements and slopes only [60]. Shape functions of the Hermitian type, when applicable, introduce undesirably high order polynomials with inherent disadvantages such as oscillations in the discrete solution and costly numerical integration (see e.g. [2, 7], among many others). Especially in the nonlinear regime, with the attendant possibility of strong gradients in the solution and costly stress-update procedures at the quadrature-point level, the computational burden associated with these approaches is particularly onerous.

The difficulties inherent in C^1 interpolation have motivated a number of alternative approaches, all of which endeavor to 'beat' the C^1 continuity requirement. Excellent reviews and insightful discussions may be found in [3, 30, 9, 28, 52, 53, 60, 54, 56, 15, 1, 50, 59, 14, 36]. C^0 elements often exhibit poor performance in the thin-shell limit — especially in the presence of severe element distortion. Such poor performance may be due to a variety of pathologies such as shear and membrane locking. The proliferation of approaches and the rapid growth of the specialized literature attest to the inherent, perhaps insurmountable, difficulties in vanquishing the C^1 continuity requirement.

A new paradigm for conforming thin-shell finite-element analysis based on *subdivision surfaces* was introduced by Cirak, Ortiz and Schöder [20]. This approach delivers–in a particularly natural and efficient manner–smooth (H^2) shape functions for the conforming finite-element discretization on general unstructured meshes of Kirchhoff-Love type shell theories. The unknowns in the finite element solution consist solely of the nodal displacements. One salient feature of the subdivision elements is the *non-locality* of the subdivision shape functions: the displacement field within one element depends on the displacements of the nodes attached to the element and the immediately adjacent nodes in the mesh. The C^1-conformity of the displacement field is automatically ensured by the use of specially designed subdivision rules. These rules can be relaxed–and adapted to–the presence of various types of boundary conditions, discontinuities in the solution, folds, and non-manifold situations such as stiffeners. For triangular elements, all element arrays may be computed by recourse to *one-point quadrature*, without consideration of any artificial stabilization procedures. The excellent accuracy and efficiency of the subdivision elements in the suite of linear test problems proposed by Belytschko *et al.* [9] was demonstrated by Cirak, Ortiz and Schöder [20].

In this paper, we extend our subdivision shell elements to the nonlinear regime. This extension takes full account of finite-deformation kinematics for compressible and incompressible materials. In contrast to the small-strain regime for large strains, the shell-thickness stretching now needs to be accounted for explicitly as part of the assumed kinematics. For thick shells, the thickness stretching can be embedded simply into the kinematics and inserted directly into three-dimensional constitutive models ([55, 15, 51, 10, 6, 50, 13] among others). For thin-shells such as considered here, the plane stress assumption may be utilized for computing the thick-

ness strain component and the corresponding change in thickness [29]. In our implementation, the thickness strain for compressible materials follows from a local Newton-Raphson iteration applied to the three-dimensional constitutive equations. For incompressible materials, the incompressibility condition yields the thickness strain directly, and the pressure follows from the plane-stress assumption [47, 24, 26, 6].

The outline of this paper is as follows: In Section 2 we introduce the shell kinematics relevant to large deformations. We begin by deriving the weak form of the static equilibrium equations for Kirchhoff-Love shell theory. Extensions to dynamic problems and the requisite time-discretization procedures are discussed subsequently. In Section 6, we briefly summarize the subdivision surface paradigm as applied by Cirak, Ortiz and Schröder [20] to the formulation of strictly C^1-continuous finite-element shape functions. Finally, we describe several examples which demonstrate the excellent performance of the method.

2   Shell kinematics

We begin with a brief summary of our assumed finite shell kinematics. Further details may be found in the standard literature [52, 54, 55, 39, 20]. We follow a conventional semi-inverse approach to the derivation of shell theories based on the formulation of an *ansatz* regarding the reduced kinematics of shell-like bodies followed by constrained minimization of the three-dimensional potential energy. An alternative approach based on rigorous energy bounds and asymptotics has been recently proposed by James and Bhattacharya [11].

Consider a shell body whose undeformed middle surface occupies a domain $\overline{\Omega} \subset \boldsymbol{R}^3$ with boundary $\partial\overline{\Omega} = \overline{\Gamma}$, and whose deformed middle surface occupies a domain $\Omega \subset \boldsymbol{R}^3$ with boundary $\partial\Omega = \Gamma$. A class of finite-deformation Kirchhoff-Love shell theories may be obtained from the *ansatz*

$$\overline{\boldsymbol{\varphi}}(\theta^1,\theta^2,\theta^3) \;\;=\;\; \overline{\boldsymbol{x}}(\theta^1,\theta^2) + \theta^3\overline{\boldsymbol{a}}_3(\theta^1,\theta^2) \quad \text{with} \quad -\frac{\overline{h}}{2} \le \theta^3 \le \frac{\overline{h}}{2} \tag{1}$$

$$\boldsymbol{\varphi}(\theta^1,\theta^2,\theta^3) \;\;=\;\; \boldsymbol{x}(\theta^1,\theta^2) + \theta^3\lambda(\theta^1,\theta^2)\boldsymbol{a}_3(\theta^1,\theta^2) \quad \text{with} \quad -\frac{\overline{h}}{2} \le \theta^3 \le \frac{\overline{h}}{2} \tag{2}$$

where $\overline{\boldsymbol{\varphi}}(\theta^1,\theta^2,\theta^3)$ is the position vector of a material point associated with the convective coordinates $\{\theta^1,\theta^2,\theta^3\}$ within the shell in its undeformed configuration. Similarly, $\boldsymbol{\varphi}(\theta^1,\theta^2,\theta^3)$ with respect to the deformed configuration of the shell. The pair $\{\theta^1,\theta^2\}$ defines a system of surface curvilinear coordinates, and the functions $\overline{\boldsymbol{x}}$ and $\boldsymbol{x}$ furnish a parametric representation of the undeformed and deformed shell middle surfaces, respectively. The remaining parameter θ^3 determines the position of a material point on the normal fiber to the undeformed middle surface $\overline{\Omega}$. The thickness stretch

$$\lambda = \frac{h}{\overline{h}} > 0 \tag{3}$$

relates the thickness h of the deformed shell to the thickness $\overline{h}$ of the undeformed shell. The mapping $\boldsymbol{\varphi} \circ \overline{\boldsymbol{\varphi}}^{-1} : \overline{\Omega} \times [-\overline{h}/2, \overline{h}/2] \to \Omega \times [-h/2, h/2]$ may be regarded as the deformation mapping of the shell body.

The covariant basis vectors on $\overline{\Omega}$ and Ω are:

$$\overline{\boldsymbol{g}}_\alpha = \frac{\partial\overline{\boldsymbol{\varphi}}}{\partial\theta^\alpha} = \frac{\partial\overline{\boldsymbol{x}}}{\partial\theta^\alpha} + \theta^3\frac{\partial\overline{\boldsymbol{a}}_3}{\partial\theta^\alpha} = \overline{\boldsymbol{a}}_\alpha + \theta^3\overline{\boldsymbol{a}}_{3,\alpha} \qquad \alpha = 1,2 \tag{4}$$

$$\overline{\boldsymbol{g}}_3 = \frac{\partial\overline{\boldsymbol{\varphi}}}{\partial\theta^3} = \overline{\boldsymbol{a}}_3 \tag{5}$$

$$\boldsymbol{g}_\alpha = \frac{\partial\boldsymbol{\varphi}}{\partial\theta^\alpha} = \frac{\partial\boldsymbol{x}}{\partial\theta^\alpha} + \theta^3\frac{\partial(\lambda\,\boldsymbol{a}_3)}{\partial\theta^\alpha} = \boldsymbol{a}_\alpha + \theta^3(\lambda\,\boldsymbol{a}_3)_{,\alpha} \qquad \alpha = 1,2 \tag{6}$$

$$\boldsymbol{g}_3 = \frac{\partial\boldsymbol{\varphi}}{\partial\theta^3} = \lambda\,\boldsymbol{a}_3 \tag{7}$$

In this and all subsequent derivations the summation convention is assumed to be in force, Latin indices range from 1 to 3 and Greek indices range from 1 to 2. The contravariant basis vectors follow from the relations

$$\overline{\boldsymbol{g}}^i \cdot \overline{\boldsymbol{g}}_j = \delta^i_j, \qquad \boldsymbol{g}^i \cdot \boldsymbol{g}_j = \delta^i_j \tag{8}$$

where δ^i_j is the Kronecker delta. For later reference, we also define the co- and contravariant metric tensors:

$$\overline{g}_{ij} = \overline{\boldsymbol{g}}_i \cdot \overline{\boldsymbol{g}}_j, \qquad \overline{g}^{ij} = \overline{\boldsymbol{g}}^i \cdot \overline{\boldsymbol{g}}^j \tag{9}$$

$$g_{ij} = \boldsymbol{g}_i \cdot \boldsymbol{g}_j, \qquad g^{ij} = \boldsymbol{g}^i \cdot \boldsymbol{g}^j \tag{10}$$

The unit normals to $\overline{\Omega}$ and Ω are:

$$\overline{\boldsymbol{a}}_3 = \frac{\overline{\boldsymbol{x}}_{,1} \times \overline{\boldsymbol{x}}_{,2}}{\overline{j}} = \frac{\overline{\boldsymbol{a}}_1 \times \overline{\boldsymbol{a}}_2}{\overline{j}} \qquad \text{and} \qquad \boldsymbol{a}_3 = \frac{\boldsymbol{x}_{,1} \times \boldsymbol{x}_{,2}}{j} = \frac{\boldsymbol{a}_1 \times \boldsymbol{a}_2}{j} \tag{11}$$

where

$$\overline{j} = |\overline{\boldsymbol{a}}_1 \times \overline{\boldsymbol{a}}_2|, \qquad j = |\boldsymbol{a}_1 \times \boldsymbol{a}_2| \tag{12}$$

are the surface Jacobians. With the aid of these definitions, the deformation gradient $\boldsymbol{F}$ for the shell body may be expressed in the form [37]

$$\boldsymbol{F} = \frac{\partial\boldsymbol{\varphi}}{\partial\overline{\boldsymbol{\varphi}}} = \frac{\partial\boldsymbol{\varphi}}{\partial\theta^i} \otimes \overline{\boldsymbol{g}}^i \tag{13}$$

In particular, for the kinematics expressed in eqs. 1 and 2 the deformation gradient follows as

$$\boldsymbol{F} = [\boldsymbol{a}_\alpha + \theta^3(\lambda\,\boldsymbol{a}_3)_{,\alpha}] \otimes \overline{\boldsymbol{g}}^\alpha + \lambda\,\boldsymbol{a}_3 \otimes \overline{\boldsymbol{g}}^3 \tag{14}$$

$$= \boldsymbol{a}_\alpha \otimes \overline{\boldsymbol{g}}^\alpha + \lambda\,\boldsymbol{a}_3 \otimes \overline{\boldsymbol{g}}^3 + \theta^3(\lambda\,\boldsymbol{a}_3)_{,\alpha} \otimes\overline{\boldsymbol{g}}^\alpha \tag{15}$$

or

$$\boldsymbol{F} = \boldsymbol{F}^{(0)} + \theta^3\boldsymbol{F}^{(1)} \tag{16}$$

where

$$\boldsymbol{F}^{(0)} = \boldsymbol{a}_\alpha \otimes \overline{\boldsymbol{g}}^\alpha + \lambda\,\boldsymbol{a}_3 \otimes \overline{\boldsymbol{g}}^3 \tag{17}$$

$$\boldsymbol{F}^{(1)} = (\lambda\,\boldsymbol{a}_3)_{,\alpha} \otimes\overline{\boldsymbol{g}}^\alpha \tag{18}$$

and the derivative of the shell director $\boldsymbol{a}_3$ follows from (11) as

$$\boldsymbol{a}_{3,\alpha} = \frac{1}{j}(\boldsymbol{a}_{1,\alpha} \times \boldsymbol{a}_2 + \boldsymbol{a}_1 \times \boldsymbol{a}_{2,\alpha}) - \frac{\boldsymbol{a}_3}{j}[(\boldsymbol{a}_{1,\alpha} \times \boldsymbol{a}_2 + \boldsymbol{a}_1 \times \boldsymbol{a}_{2,\alpha}) \cdot \boldsymbol{a}_3] \tag{19}$$

3   Weak form of the governing equations

In preparation for the introduction of the finite element discretization, we proceed to formulate the equations of motion of the shell body in weak form. In he static case, the potential energy of the shell body takes the form:

$$\Pi[\boldsymbol{\varphi}] = \int_{\overline{\Omega}} \int_{-\frac{h}{2}}^{\frac{\overline{h}}{2}} W(\boldsymbol{F}) \, \mu \, d\overline{\Omega} \, d\theta^3 + \Pi_{ext} \equiv \Pi_{int} + \Pi_{ext} \tag{20}$$

where, for an elastic material, W is the strain-energy density per unit undeformed volume, Π_{ext} is the potential of the externally applied forces, and

$$\mu = \frac{|(\overline{\boldsymbol{g}}_1 \times \overline{\boldsymbol{g}}_2) \cdot \overline{\boldsymbol{g}}_3|}{|(\overline{\boldsymbol{a}}_1 \times \overline{\boldsymbol{a}}_2) \cdot \overline{\boldsymbol{a}}_3|} \tag{21}$$

accounts for the curvature of the shell in the computation of the element of volume. At equilibrium the potential energy of the shell body is stationary, i. e.,

$$\delta\Pi = \delta\Pi_{int} + \delta\Pi_{ext} = 0 \tag{22}$$

Here

$$\delta\Pi_{int} = \int_{\overline{\Omega}} \int_{-\frac{h}{2}}^{\frac{\overline{h}}{2}} \frac{\partial W}{\partial \boldsymbol{F}} : \delta\boldsymbol{F} \, \mu \, d\overline{\Omega} \, d\theta^3 = \int_{\overline{\Omega}} \int_{-\frac{h}{2}}^{\frac{\overline{h}}{2}} \boldsymbol{P} : \delta\boldsymbol{F} \, \mu \, d\overline{\Omega} \, d\theta^3 \tag{23}$$

where $\boldsymbol{P}$ is the first Piola-Kirchhoff stress tensor. Introduction of the assumed shell kinematics (14) into (23) leads to the internal virtual work expression:

$$\begin{aligned}
\delta\Pi_{int} &= \int_{\overline{\Omega}} \int_{-\frac{h}{2}}^{\frac{\overline{h}}{2}} \boldsymbol{P} : [\delta\boldsymbol{a}_\alpha \otimes \overline{\boldsymbol{g}}^\alpha + \lambda \, \delta\boldsymbol{a}_3 \otimes \overline{\boldsymbol{g}}^3 + \theta^3 (\lambda \, \delta\boldsymbol{a}_3)_{,\alpha} \otimes \overline{\boldsymbol{g}}^\alpha] \, \mu \, d\overline{\Omega} \, d\theta^3 \\
&+ \int_{\overline{\Omega}} \int_{-\frac{h}{2}}^{\frac{\overline{h}}{2}} \boldsymbol{P} : [\delta\lambda \, \boldsymbol{a}_3 \otimes \overline{\boldsymbol{g}}^3 + \theta^3 (\delta\lambda \, \boldsymbol{a}_3)_{,\alpha} \otimes \overline{\boldsymbol{g}}^\alpha] \, \mu \, d\overline{\Omega} \, d\theta^3
\end{aligned} \tag{24}$$

or, introducing the Kirchhoff stress tensor $\boldsymbol{\tau} = \boldsymbol{P}\boldsymbol{F}^T$,

$$\begin{aligned}
\delta\Pi_{int} &= \int_{\overline{\Omega}} \int_{-\frac{h}{2}}^{\frac{\overline{h}}{2}} \boldsymbol{\tau} : [\delta\boldsymbol{a}_\alpha \otimes \boldsymbol{g}^\alpha + \lambda \, \delta\boldsymbol{a}_3 \otimes \boldsymbol{g}^3 + \theta^3 (\lambda \, \delta\boldsymbol{a}_3)_{,\alpha} \otimes \boldsymbol{g}^\alpha] \, \mu \, d\theta^3 d\overline{\Omega} \\
&+ \int_{\overline{\Omega}} \int_{-\frac{h}{2}}^{\frac{\overline{h}}{2}} \boldsymbol{\tau} : [\delta\lambda \, \boldsymbol{a}_3 \otimes \boldsymbol{g}^3 + \theta^3 (\delta\lambda \, \boldsymbol{a}_3)_{,\alpha} \otimes \boldsymbol{g}^\alpha] \, \mu \, d\theta^3 d\overline{\Omega}
\end{aligned} \tag{25}$$

Additionally, since the variations $\delta\boldsymbol{x}$ and $\delta\lambda$ are independent, (22) decouples into the equations:

$$\int_{\overline{\Omega}} \int_{-\frac{h}{2}}^{\frac{\overline{h}}{2}} \boldsymbol{\tau} : [\delta\boldsymbol{a}_\alpha \otimes \boldsymbol{g}^\alpha + \lambda \, \delta\boldsymbol{a}_3 \otimes \boldsymbol{g}^3 + \theta^3 (\lambda \, \delta\boldsymbol{a}_3)_{,\alpha} \otimes \boldsymbol{g}^\alpha] \, \mu \, d\theta^3 d\overline{\Omega} + \delta\Pi_{ext} = 0 \tag{26}$$

$$\int_{\overline{\Omega}} \int_{-\frac{h}{2}}^{\frac{\overline{h}}{2}} \boldsymbol{\tau} : [\delta\lambda \, \boldsymbol{a}_3 \otimes \boldsymbol{g}^3 + \theta^3 (\delta\lambda \, \boldsymbol{a}_3)_{,\alpha} \otimes \boldsymbol{g}^\alpha] \, \mu \, d\theta^3 d\overline{\Omega} = 0 \tag{27}$$

The first of these equations establishes the equilibrium of the middle surface of the shell, whereas the second equation enforces equilibrium across the shell thickness. Eq. (26) may be simplified by the introduction of the stress and moment resultants:

$$\boldsymbol{n}^i = \int_{-\frac{\overline{h}}{2}}^{\frac{\overline{h}}{2}} \boldsymbol{\tau} \cdot \boldsymbol{g}^i \, \mu \, d\theta^3 \tag{28}$$

$$\boldsymbol{m}^\alpha = \int_{-\frac{\overline{h}}{2}}^{\frac{\overline{h}}{2}} \boldsymbol{\tau} \cdot \boldsymbol{g}^\alpha \theta^3 \, \mu \, d\theta^3 \tag{29}$$

whereupon (26) becomes

$$\int_{\overline{\Omega}} [\boldsymbol{n}^\alpha \cdot \delta \boldsymbol{a}_\alpha + \lambda \, \boldsymbol{n}^3 \cdot \delta \boldsymbol{a}_3 + \boldsymbol{m}^\alpha \cdot (\lambda \, \delta \boldsymbol{a}_3)_{,\alpha}] \, \mu \, d\overline{\Omega} + \delta \Pi_{ext} = 0 \tag{30}$$

In dynamical problems, (30) is augmented by the addition of inertia forces, with the result:

$$\int_{\overline{\Omega}} [\boldsymbol{n}^\alpha \cdot \delta \boldsymbol{a}_\alpha + \lambda \, \boldsymbol{n}^3 \cdot \delta \boldsymbol{a}_3 + \boldsymbol{m}^\alpha \cdot (\lambda \, \delta \boldsymbol{a}_3)_{,\alpha}] \, \mu \, d\overline{\Omega} + \delta \Pi_{ext} + \int_{\overline{\Omega}} \overline{\rho} \, \overline{h}^* \, \ddot{\boldsymbol{x}} \cdot \delta \boldsymbol{x} \, d\overline{\Omega} = 0 \tag{31}$$

where $\overline{\rho}$ is the mass density per unit undeformed volume and

$$\overline{h}^* = \int_{-\frac{\overline{h}}{2}}^{\frac{\overline{h}}{2}} \mu \, d\theta^3 \tag{32}$$

For simplicity, in writing (31) we have assumed that the rotational inertial of the shell is small, as may be expected to be the case for very thin shells, and can be safely neglected.

4   Constitutive models

In this section we give a brief description of the material models employed in the numerical examples discussed subsequently. While we restrict our discussion to hyperelastic solids, the methodology herein described carries over to plastic materials within the incremental variational framework proposed by Stainier and Ortiz [44].

As an example of compressible hyperelastic behavior, we consider a Neo-Hookean material [42] extended to the compressible range. The behavior of the material is characterized by a strain energy density per unit undeformed volume of the form

$$W(\boldsymbol{C}) = \frac{\lambda_0}{2} (\log J)^2 - \mu_0 \log J + \frac{\mu_0}{2} (\text{tr}\boldsymbol{C} - 3) \tag{33}$$

where λ_0 and μ_0 are material parameters,

$$J = \det(\boldsymbol{F}) = \sqrt{\frac{\det(\boldsymbol{g})}{\det(\overline{\boldsymbol{g}})}} \tag{34}$$

is the Jacobian of the deformation and

$$\boldsymbol{C} = \boldsymbol{F}^T \boldsymbol{F} = g_{ij} \, \overline{\boldsymbol{g}}^i \otimes \overline{\boldsymbol{g}}^j \tag{35}$$

is the right Cauchy-Green deformation tensor. The Kirchhoff stresses follow from W by an application of the Doyle-Ericksen relation [37], with the result:

$$\tau^{ij} = 2\frac{\partial W}{\partial g_{ij}} = (\lambda_0 \log J - \mu_0)g^{ij} + \mu_0 \overline{g}^{ij} \tag{36}$$

The tangent moduli in turn follow by linearization in the form:

$$C^{ijkl} = 4\frac{\partial^2 W}{\partial g_{ij}\partial g_{kl}} = \lambda_0 g^{ij} \otimes g^{kl} + 2(\lambda_0 \log J - \mu_0)g^{ij} \otimes g^{kl} \tag{37}$$

As an example of incompressible hyperelastic behavior, we consider a Mooney-Rivlin material, characterized by the strain energy density per unit undeformed volume:

$$W(\boldsymbol{C}) = c_1(I_1 - 3) + c_2(I_2 - 3) \tag{38}$$

where c_1 and c_2 are material constants, and I_1 and I_2 are the first and second invariants of the right Cauchy-Green tensor $\boldsymbol{C}$, respectively. As before, the Doyle-Ericksen relation delivers the Kirchhoff stress in the form:

$$\tau^{ij} = 2\frac{\partial W}{\partial g_{ij}} = 2(c_1 + c_2\overline{g}^{kl}g_{kl})\overline{g}^{ij} - 2c_2\overline{g}^{ik}g_{kl}\overline{g}^{lj} - pg^{ij} \tag{39}$$

where p denotes the hydrostatic pressure.

Finally, we enforce the plane stress condition strongly by requiring that

$$\tau^{33} = 2\frac{\partial W}{\partial g_{33}} = 0 \tag{40}$$

pointwise across the thickness of the shell. Here, as before, all components are taken relative to the local surface basis $\{\boldsymbol{g}_1, \boldsymbol{g}_2, \boldsymbol{g}_3\}$, and thus τ^{33} is the axial stress in the direction of the deformed shell normal. The plane stress condition (40) may conveniently be enforced at the constitutive level. To this end, we additionally have, by virtue of the assumed shell kinematics, that $g_{\alpha 3} = g_{3\alpha}$ are zero. The value of g_{33} may be computed from (40) numerically, e. g., by a Newton-Raphson iteration. The thickness stretch is then recovered as:

$$\lambda = \frac{1}{\overline{h}}\int_{-\frac{\overline{h}}{2}}^{\frac{\overline{h}}{2}} \sqrt{g_{33}} \quad d\theta^3 \tag{41}$$

A similar approach for enforcing the plane-stress constraint in the context of elastic-plastic behavior has been discussed by De Borst [22].

For incompressible materials the thickness stretch follows directly from the incompressibility condition [47]

$$\det(\boldsymbol{F}) = \sqrt{\frac{\det(\boldsymbol{g})}{\det(\overline{\boldsymbol{g}})}} = 1 \tag{42}$$

with the result:

$$g_{33} = \frac{\det(\overline{\boldsymbol{g}})}{g_{11}g_{22} - g_{12}g_{21}} \tag{43}$$

The unknown pressure p in (39) may then be computed directly from the plane-stress constraint as

$$p = 2(c_1 + c_2\overline{g}^{kl}g_{kl}) - 2c_2\overline{g}^{3k}g_{kl}\overline{g}^{l3} \tag{44}$$

5   Spatial and temporal discretization

Subdivision schemes such as discussed in Section 6 have the property that the interpolating displacement fields are entirely determined by the displacements at the vertices of a triangulation of the shell, or *control mesh*. In particular, no rotation degrees-of-freedom need to be carried at the nodes. This results in the particularly simple representation:

$$\overline{\boldsymbol{x}}_h = \sum_{I=1}^{NP} N^I \overline{\boldsymbol{x}}_I, \qquad \boldsymbol{x}_h = \sum_{I=1}^{NP} N^I \boldsymbol{x}_I \tag{45}$$

for the undeformed and deformed middle surfaces of the shell, respectively. In (45), $N^I, I = 1, ..., NP$ are C^1 shape functions, to be defined in Section 6, $\overline{\boldsymbol{x}}_I$ and $\boldsymbol{x}_I$ are the nodal coordinates of the undeformed and deformed middle surfaces of the shell, and NP is the total number of the nodes in the mesh. The C^1 property of the shape functions is also ensured by the use of subdivision schemes. In addition, the interpolated parametric equations $\boldsymbol{x}_h$ of the shell middle surface belong to the Sobolev space of functions $H^2(\overline{\Omega}, R^3)$ and can, therefore, be inserted as test functions into the Kirchhoff-Love potential energy.

Introduction of discretization (45) into the weak form (31) yields a semi-discrete system of equations of the form:

$$\boldsymbol{M}_h \ddot{\boldsymbol{x}}_h + \boldsymbol{f}_h^{int}(\boldsymbol{x}_h) = \boldsymbol{f}_h^{ext}(t) \tag{46}$$

where $\boldsymbol{M}_h$ is the mass matrix, $\boldsymbol{f}_h^{int}(\boldsymbol{x}_h)$ is the internal force array, and $\boldsymbol{f}_h^{ext}(t)$ is the external force array. The internal forces $\boldsymbol{f}_I^{int}$ at node I follow in the form:

$$\boldsymbol{f}_I^{int} = \int_{\overline{\Omega}} [\boldsymbol{n}^\alpha \cdot \frac{\partial \boldsymbol{a}_\alpha}{\partial \boldsymbol{x}_I} + \lambda\,\boldsymbol{n}^3 \cdot \frac{\partial \boldsymbol{a}_3}{\partial \boldsymbol{x}_I} + \boldsymbol{m}^\alpha \cdot (\lambda \frac{\partial \boldsymbol{a}_3}{\partial \boldsymbol{x}_I})_{,\alpha}\,]\,\mu\,d\overline{\Omega} \tag{47}$$

As in the standard finite element method, the global internal force array is the sum of element contributions, each of which entails the computation of an integral extended to the domain of one element. For the subdivision shape functions defined in Section 6, corresponding to three-node triangular elements, the element integrals can be computed by a *one-point* quadrature rule. The internal forces contributed by a generic element are, therefore, of the form:

$$\boldsymbol{f}_I^{int} = \left\{ \left[\boldsymbol{n}^\alpha \cdot \frac{\partial \boldsymbol{a}_\alpha}{\partial \boldsymbol{x}_I} + \lambda\,\boldsymbol{n}^3 \cdot \frac{\partial \boldsymbol{a}_3}{\partial \boldsymbol{x}_I} + \boldsymbol{m}^\alpha \cdot (\lambda \frac{\partial \boldsymbol{a}_3}{\partial \boldsymbol{x}_I})_{,\alpha} \right] \mu\,\overline{j} \right\}_{(\theta_G^1, \theta_G^2)} w_G \tag{48}$$

where (θ_G^1, θ_G^2) are the surface coordinates of the barycenter of the element and w_G is the corresponding Gaussian quadrature weight. We additionally compute the stress resultants $\boldsymbol{n}^i$ and $\boldsymbol{m}^\alpha$ by numerical integration of the stresses across the thickness of the shell using Simpson's rule. The mass matrix follows likewise as

$$M_{IJ} = \int_\Omega \int_{-\frac{\overline{h}}{2}}^{\frac{\overline{h}}{2}} \rho N^I N^J\,\mu\,d\theta^3 d\overline{\Omega} \tag{49}$$

As in the calculation of the force resultants, the integral across the thickness of the shell is computed numerically using Simpson's rule. The semidiscrete equations of motion (46) are further discretized in time by recourse to the explicit Newmark scheme (e. g. [8]). In calculations we use a lumped mass matrix computed by the row-sum procedure.
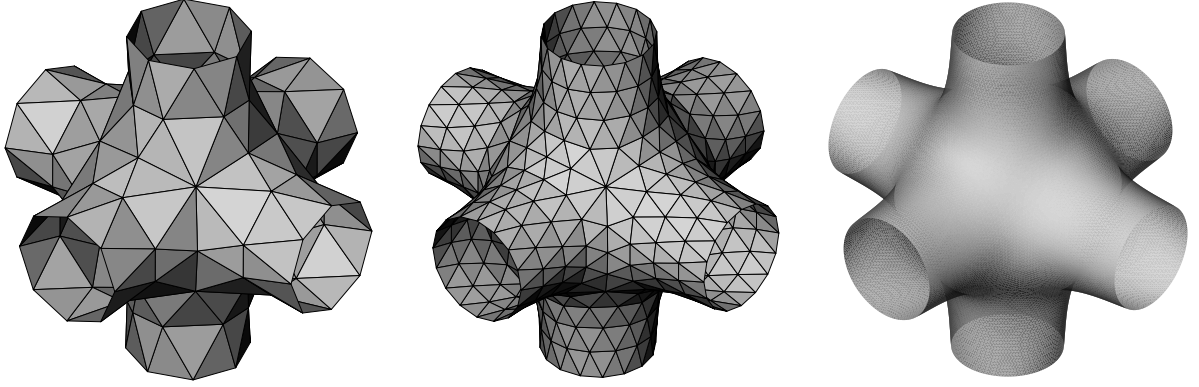
Figure 1: Pipe connection: Control mesh, first subdivided mesh, and the limit surface.

6   Discretization with subdivision surfaces

Cirak, Ortiz and Schröder [20] have recently proposed a new paradigm for C^1-interpolation based on subdivision surfaces and applied it to Kirchhoff-Love shell analysis. In this section, we briefly review the basic procedure for the sake completeness. The reader interested in subdivision surfaces, specially as regards applications to geometrical modeling and computer graphics, is referred to the standard literature on the subject [61, 12, 62, 48, 16, 23].

Our discussion is restricted to primal subdivision schemes and triangular meshes. An extension to dual subdivision schemes and quadrilateral meshes may be found elsewhere [21]. Subdivision schemes construct a smooth surface through a limiting procedure of repeated refinement, starting from an initial or *control* mesh. Every iteration of the procedure consists of two steps. Firstly, the mesh is refined by quadrisection of all elements. Secondly, new nodal positions are computed as a linear combination of the old nodal positions of the unrefined mesh. Fig. 1 shows an application of the subdivision method to a pipe connection. The coarse control mesh which sets the initial condition for the subdivision procedure is shown on the left of the figure. By repeated application of a subdivision scheme, the surface converges to the smooth continuous limit surface shown on the right. The particular subdivision scheme applied in this example, as well as elsewhere in this paper, is Loop's scheme [35].

The valence of a node is the number of edges incident on the node. A vertex is said to be regular if its valence is six, i. e., if six edges are incident on the vertex, and it is said to be irregular otherwise. The limit surface obtained by the application of Loop's scheme is C^2-continuous at regular vertices and C^1-continuous at irregular vertices. Overall, the limit subdivision surface is shown by Reif and Schröder [49] to posses square integrable curvatures, consequently, it may be used as a trial finite element solution in the context of the Kirchhoff-Love theory of shells. The subdivision process is strictly local and, following a subdivision step, the new coordinates of a vertex depend solely on the previous coordinates of a small number of neighboring vertices. Using the indexing depicted in Fig. 2, the coordinates of the new vertices $\boldsymbol{x}_0^1, \boldsymbol{x}_1^1, \boldsymbol{x}_2^1, \cdots$ generated on the edges of the previous mesh follow as:

$$\boldsymbol{x}_I^{k+1} = \frac{3\boldsymbol{x}_c^k + \boldsymbol{x}_{I-1}^k + 3\boldsymbol{x}_I^k + \boldsymbol{x}_{I+1}^k}{8} \qquad I = 0, \ldots, N-1 \tag{50}$$

where the label k is the subdivision iteration index, or subdivision level, N is the valence of the

vertex, and the index I is taken modulo N. The vertices already contained in the previous mesh are assigned new nodal positions:

$$\boldsymbol{x}_c^{k+1} = (1 - Nw)\boldsymbol{x}_c^k + w\boldsymbol{x}_0^k + \cdots + w\boldsymbol{x}_{N-1}^k \tag{51}$$

with

$$w = \frac{1}{N}\left[\frac{5}{8} - \left(\frac{3}{8} + \frac{1}{4}\cos\frac{2\pi}{N}\right)^2\right] \tag{52}$$

This value of the weight w is as originally proposed by Loop [35]. Alternative choices based on a smoothness analysis are also possible [48, 12]. The action of the subdivision operator may conveniently be described algebraically as a matrix-vector multiplication (see, e. g., [20]).

For regular elements, all of whose nodes are vertices of valence six, Loop's scheme returns Box-splines in the limit and the surface can be interpolated directly by means of Box-spline shape functions, as discussed in [20]. The position and the derivatives of the limit surface within regular elements can thus be evaluated directly. The parameterization of subdivision surfaces in the vicinity of irregular patches (Fig. 3) was an open question until recently. In [58, 57], Stam has proposed a simple parameterization for irregular patches which has effectively resolved this question. Stam's parameterization is based on the general observation that all vertices generated by subdivision are regular. Accordingly, after a sufficient number of subdivision steps each vertex in the mesh is contained within a regular patch to which the Box-spline parameterization may be applied.

A particularly appealing feature of the triangular subdivision shell elements proposed by Cirak, Ortiz and Schröder [20] is that they only require one quadrature point for the calculation of the element arrays. Consequently, the position vector of the deformed shell and its first and second derivatives need only be computed at the barycenter of each element. A complete algorithm for computing the shape functions and their first and second derivatives at the barycenter of an element has been given in [20]. All items of interest follow simply as a function of the nodal displacement at the control vertices of the element under consideration, as well as the nodal displacements at the one-ring of neighboring control vertices, Fig. 3. It should be carefully noted that the subdivision method guarantees that all such patches match exactly over their
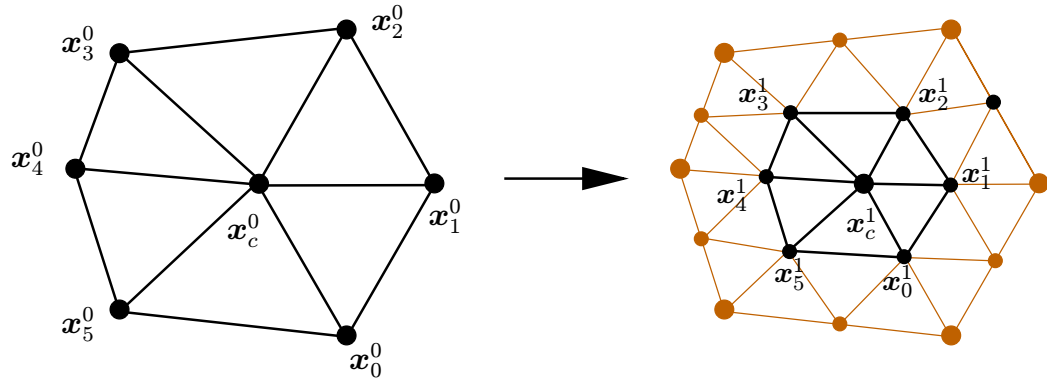

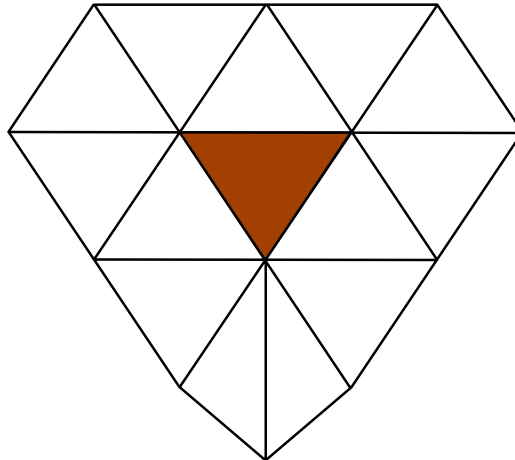Figure 2: Refinement of a triangular mesh by quadrisection.

Figure 3: Triangular element and its control nodes.

regions of overlap, and the limiting surface is uniquely defined. It also bears emphasis that sub-division elements carry displacements at the vertices only, unlike other interpolation schemes which make use of other types of nodal variables such as rotations. This feature of subdivision elements greatly facilitates their compatibility with solid elements, among other advantages.

7 Examples

In this section we investigate the performance of subdivision shell elements in the finite-deformation range. All computations are performed using one-point Gaussian quadrature over the shell middle surface and the three-point Simpson rule for integration across the shell thickness. No numerical instabilities attributable to underintegration of the elements have been observed. The static solutions are computed by dynamic relaxation (e. g. [41, 46]).

7.1 Tension strip

Our first verification test concerns a square Neo-Hookean plate undergoing a large uniaxial stretch. The exact solution consists of a uniform state of uniaxial extension accompanied by a uniform thickness reduction. The test is thus in the spirit of a conventional patch test. In the calculations reported here, the shear modulus μ_0 is normalized to 1, whereas the Lamè constant λ_0 is assigned four different values ranging from 0 to 3. In Fig. 4, the computed dependence of the Cauchy stresses and the thickness stretch λ on the prescribed in-plane stretch is compared to the exact values obtained directly from the constitutive law. The ability of the element to account for thickness deformation is evident from the figure.

7.2 Inflation of a sphere

Our next example concerns the inflation of a spherical incompressible shell under the action of internal pressure. This problem is amenable to analytical solution [40, 42, 26] and, therefore,
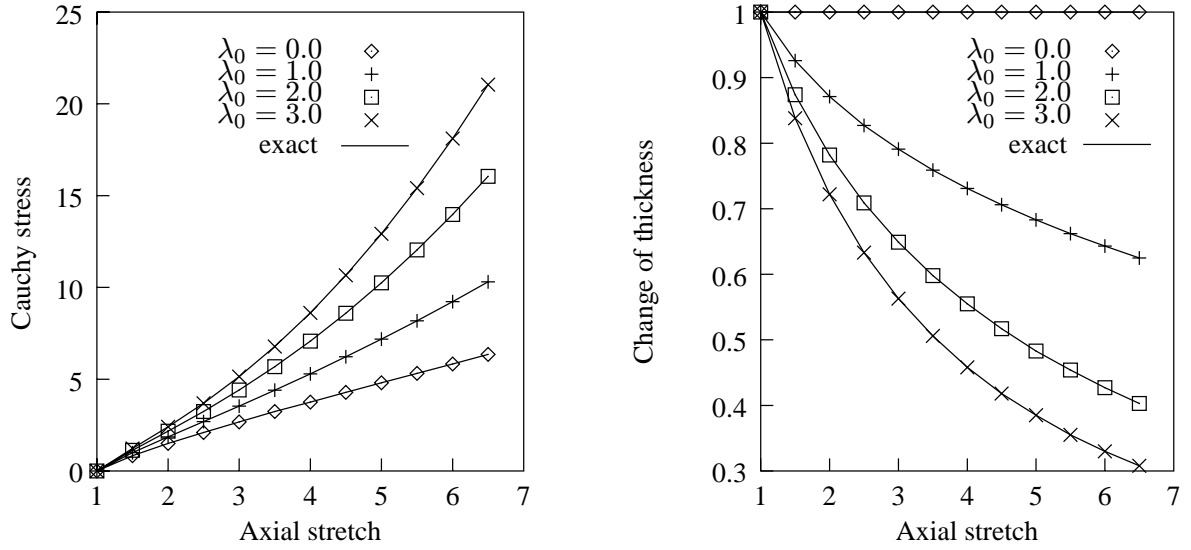
Figure 4: Simple tension test for the Neo-Hookean plate: a) Comparison of exact and computed variation of axial Cauchy stress with applied stretch. b) Comparison of exact and computed variation in plate thickness with applied stretch.

provides a convenient basis for the assessment of the accuracy and convergence properties of the subdivision shell element. The relation between the internal pressure and the radial stretch ratio $\gamma = R/\overline{R}$ follows from equilibrium as:

$$p = \frac{\overline{h}}{\overline{R}\gamma^2} \frac{dW}{d\gamma} \tag{53}$$

Here $\overline{R}$ is the radius of the undeformed middle surface of the shell, R is the corresponding radius for the deformed shell, and W is the strain-energy density of the material per unit undeformed volume. For the Mooney-Rivlin material, eq. (38), the relation (53) specializes to:

$$p = \frac{4\overline{h}}{\overline{R}\gamma^2}(\gamma^6 - 1)(c_1 + c_2\gamma^2) \tag{54}$$

where c_1 and c_2 are material constants.

The problem of the inflation of a sphere tests the performance of the subdivision element under conditions of large membrane deformations. However, it should be carefully noted that the inflation of the sphere entails a change of curvature as well, even though this change in curvature does not result in bending strains or bending moments. Consequently, the problem of the inflation of a sphere also tests the proper handling of subtle aspects of finite-deformation shell kinematics such as the interdependence between curvature, stretching, bending strains and membrane strains.

In calculations we set the undeformed shell radius to 1, the undeformed thickness-to-radius ratio to $\overline{h}/\overline{R} = 0.02$, and the Mooney-Rivlin material constants to $c_1 = 20$ and $c_2 = 10$. The internal pressure ranges from 0 to 4. Whereas the discretization of the complete sphere permits bifurcations away from the spherical solution, as described by Needleman [40], for the range of parameters explored here such bifurcations do not arise and the solution remains spherical at
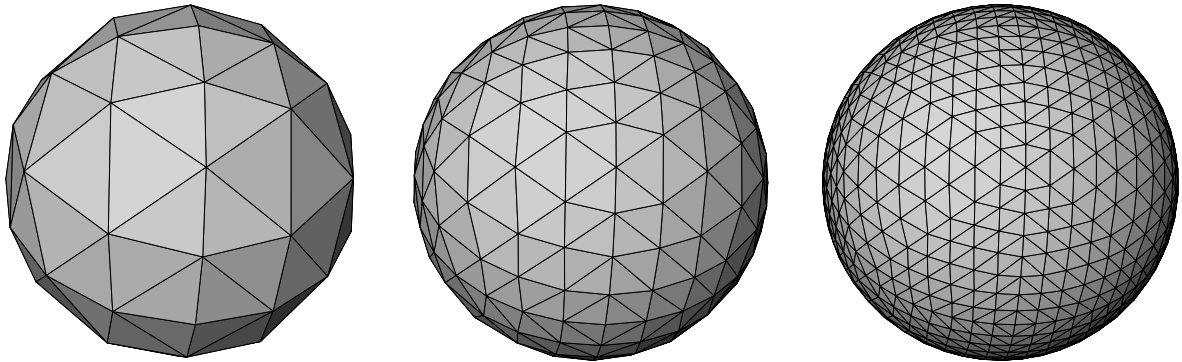
Figure 5: Inflation of a Mooney-Rivlin sphere. Control meshes used in calculations containing 128, 512, and 2048 elements

all times. The shell thins down considerably as it expands, and at maximum expansion the ratio h/R reduces to 0.0009, which places the shell well into the thin-shell range.

The three control meshes used in the calculations, containing 128, 512, and 2048 elements, respectively, are shown in Fig. 5. Fig. 6 compares the exact pressure-radial expansion curve against the three numerical solutions. The good accuracy obtained with the coarsest mesh and the general trend towards convergence are noteworthy in this figure.

7.3   Bending and inflation of a circular plate

As a simple test of the subdivision elements under combined membrane and bending conditions we consider the problem of bending of a simply-supported circular plate under uniform pressure. Initially, the plate is relatively thick, with a radius of 7.5 and a thickness of 0.5, or a radius-to-thickness ratio of 15. The Mooney-Rivlin material parameters c_1 and c_2 are set to 80 and 20, respectively. The control mesh used in calculations is shown in Fig. 7a. The mesh contains 548 triangular elements and is generated by Delaunay triangulation followed by one subdivision step in order to separate irregular vertices [20]. Fig. 8 compares the computed dependence of the center deflection on the applied pressure with the finite-element solution of Hughes and Carnoy [29]. This latter solution was obtained using approximately nine nine-node elements over the radius and contains more degrees of freedom than our discretization. As may be observed in Fig. 8, the agreement between both solutions is excellent. Also shown in Fig. 7 is the computed deflected shape of the plate at a pressure $p = 35$. The extent of the deflections undergone by the plate, and the high degree of smoothness in the solution afforded by the subdivision method, are particularly noteworthy is this figure.

7.4   Inflation of airbags

We conclude this section with an application of the subdivision elements to the problem of inflation of airbags. This problem furnishes an example of finitely-deforming very thin shells. Owing to this extreme thinness, some analysts have neglected the effect of bending and idealized airbags as membranes [27]. Indeed, for commonly employed materials the membrane stiffness of airbags is much larger than its bending stiffness. In addition, the degree of stretching of
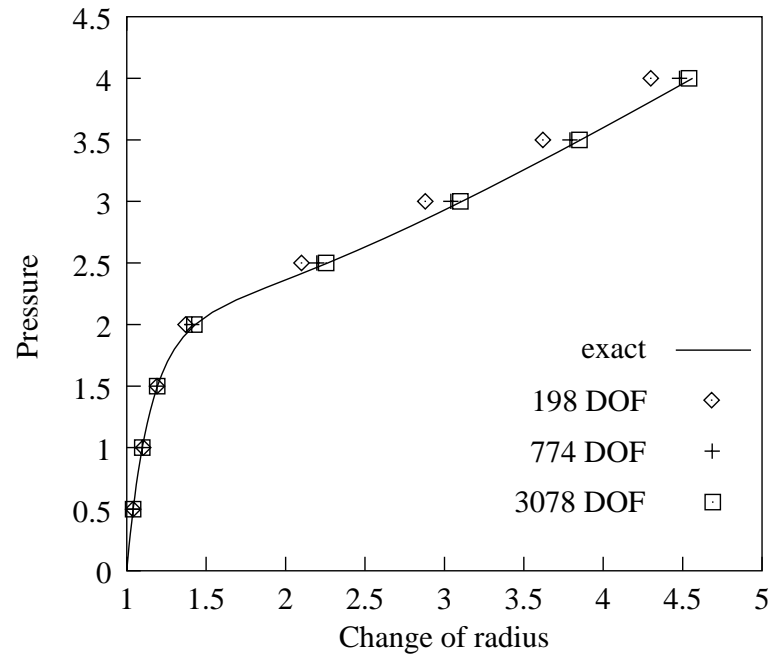
Figure 6: Inflation of a Mooney-Rivlin sphere. Comparison of exact and computed pressure-radial expansion curve.
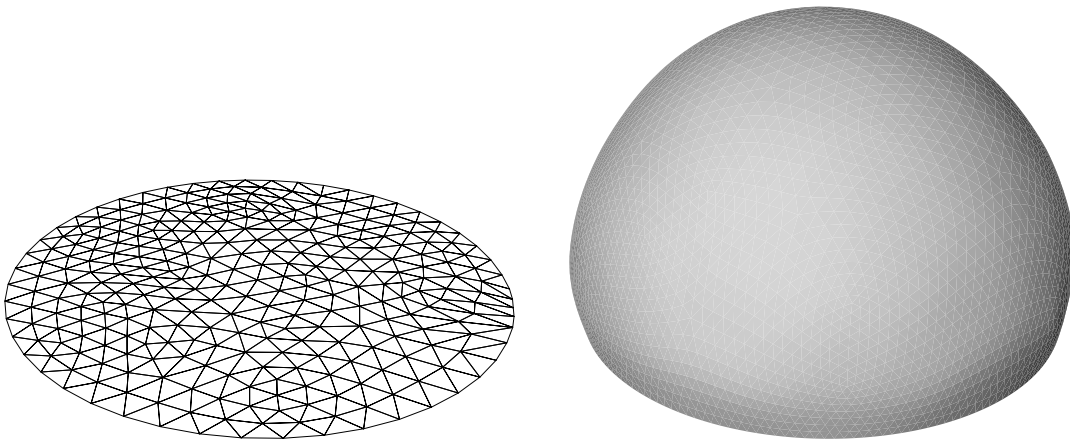

Figure 7: Mooney-Rivlin simply-supported circular plate under uniform pressure. a) Control mesh. b) Deflected shape at pressure $p = 35$.
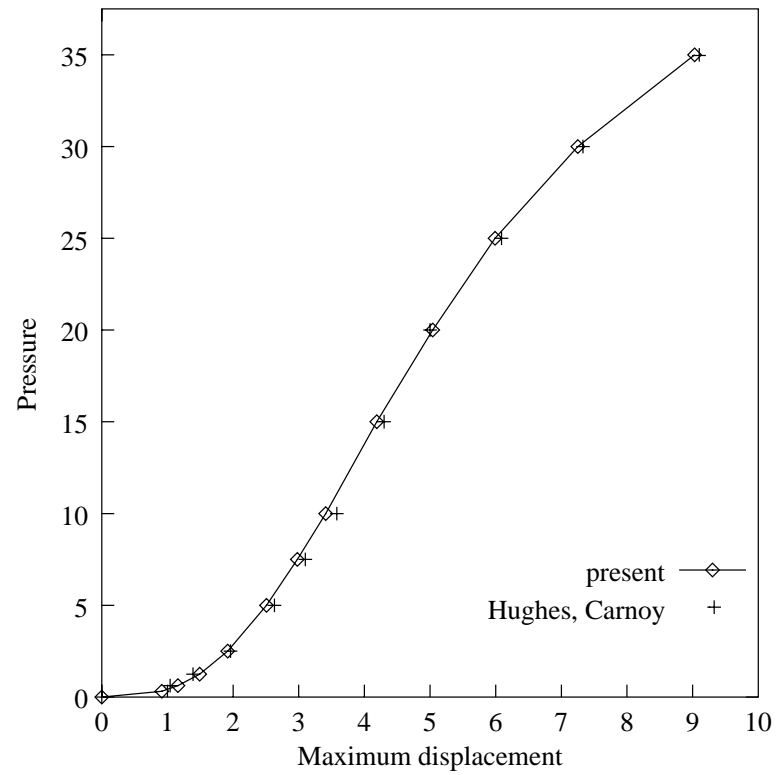
Figure 8: Mooney-Rivlin simply-supported circular plate under uniform pressure. Pressure *vs*. center deflection. Comparison between subdivision solution and Hughes and Carnoy's solution [29].

the airbag is often small and the airbag may additionally be idealized as inextensible to a first approximation.

However, the bending energy does play a crucial role in the determination of the fine folding pattern of the shell, including the arrangement of folds, or wrinkles, and their number and size [45, 43, 25, 17]. Indeed, under static conditions the mechanics of the inflation of an inextensible airbag may be understood as a competition between the potential energy of the applied pressure, which is proportional to the volume of the bag, and bending energy. The former strives to maximize the volume enclosed by the airbag, which vanishes initially, and thus favors fine folding. The latter strives to minimize the number of folds in the deflection pattern. Indeed, in the so-called sharp-interface approximation to bending [38, 32, 43, 25, 31] the fold ridges and troughs are the sole carriers of bending energy. The preferred folding pattern may be expected to coincide with the absolute minimizer of the total energy and, therefore, to be a compromise between the opposing demands of the internal pressure and bending energy.

It should be noted that, in the absence of the bending regularization, the absolute energy minimizer may exhibit infinitely fine folding and be massively non-unique, owing to the local and strongly nonconvex character of the energy functional [45, 43, 25]. The inclusion of bending has a regularizing effect and leads to a singularly perturbed nonconvex minimization problem [43, 25, 31]. Even with bending taken into account, examples of multiple folding patterns returning the same total minimum energy have been given by Jin [31] for the problem of compressed thin-film buckling. These examples demonstrate the lack of uniqueness of the absolute energy minimizers. In addition, the regularized energy may be expected to have numerous metastable local minima in the form of stable equilibrium deflections whose energy exceeds the minimum attainable energy.

In calculations we consider airbags of square and circular deflated shapes, and take full account of their membrane and bending energies. For the square airbag, the deflated diagonal length is 1.20 and its thickness is 0.001. The material is Neo-Hookean with a Young's modulus $E = 5.88 \times 10^8$ and a Poisson's ratio $\nu = 0.4$. Four meshes of increasing refinement containing 1635, 6339 and 24963 degrees of freedom are considered. The radius of the circular airbag in its undeflected configuration is 0.35 and its thickness is 0.0004. The material is Neo-Hookean with Young's modulus $E = 6 \times 10^7$ and Poisson's ratio $\nu = 0.3$. We consider five different discretizations of the circular airbag with 507, 1851, 7029, 27555, and 108867 degrees of freedom. The coarsest control meshes used in the calculations are shown in Fig. 9. As before, in constructing these and all other meshes a first mesh is obtained by Delaunay triangulation followed by quadrisection of all triangles in order to separate irregular nodes. In all cases, the perimeter of the airbag is constrained in the direction normal to the plane of the deflated bag, but is otherwise unconstrained. The objective of the calculation is to determine the quasistatic deformed shape of the airbags when pressurized to $p = 5000$.

The computed folded configurations of the airbags are shown in Figs. 10 and 11. As expected, coarse meshes inhibit folding. Conversely, mesh refinement is accompanied by an increase in the fineness of the folding pattern. The ability of the subdivision elements to capture increasingly fine and intricate detail in the deflected shape of very thin shells under strongly nonlinear conditions, and the smoothness of all computed deformed surfaces, are particularly noteworthy. Whereas, as noted earlier, the deflected pattern of the airbag is non-unique, some average or aggregate aspects of the solution may be expected to converge properly as the mesh is refined. By way of example, Fig. 12 shows the computed maximum displacement at the cen-
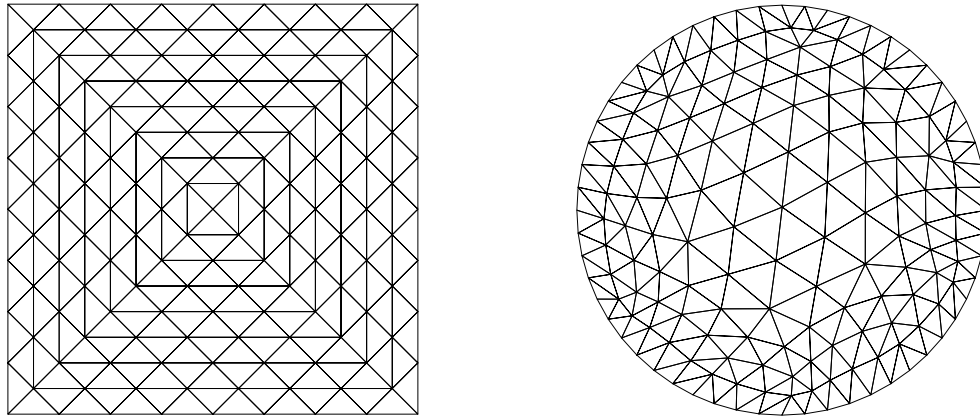
Figure 9: Neo-Hookean airbag problem. Coarse control meshes before quadrisection. a) Square airbag. b) Circular airbag.

ter of the bag *vs* the number of degrees of freedom. Evidently, for an inextensible airbag the maximum deflection is necessarily bounded, and thus may be expected to converge, possibly up to subsequences, as the mesh is refined. This trend towards convergence is clearly evident in Fig. 12.

8   Summary and conclusions

We have extended the subdivision shell elements of Cirak, Ortiz and Schröder [20] to the finite-deformation range. The assumed finite-deformation kinematics allows for finite membrane and thickness stretching, as well as for large deflections and bending strains. The interpolation of the undeformed and deformed surfaces of the shell is accomplished through the use of subdivision surfaces. The resulting 'subdivision elements' are strictly C^1-conforming, contain three nodes and one single quadrature point per element, and carry displacements at the nodes only. The versatility and good performance of the subdivision elements has been demonstrated with the aid of a number of test cases, including the stretching of a tension strip; the inflation of a spherical shell under internal pressure; the bending and inflation of a circular plate under the action of uniform pressure; and the inflation of square and circular airbags.

   As noted in [20], subdivision surfaces enable the finite-element analysis of thin shells to be carried out within the strict framework of Kirchhoff-Love theory while meeting all the convergence requirements of the displacement finite-element method, thereby sidestepping the difficulties associated with the use of C^0 methods in the limit of very thin-shells. In particular, for elastic materials the finite-element solution follows by constrained minimization of the potential energy of the shell over the space of interpolated displacement fields, in the spirit of Rayleigh and Ritz. For linear problems, finite-element methods formulated in accordance with this prescription possess the orthogonality and the best-approximation properties, i. e., the error is orthogonal to the space of finite-element interpolants and the finite-element solution minimizes the distance to the exact solution in the energy norm. These properties confer great robustness to the direct finite-element method.

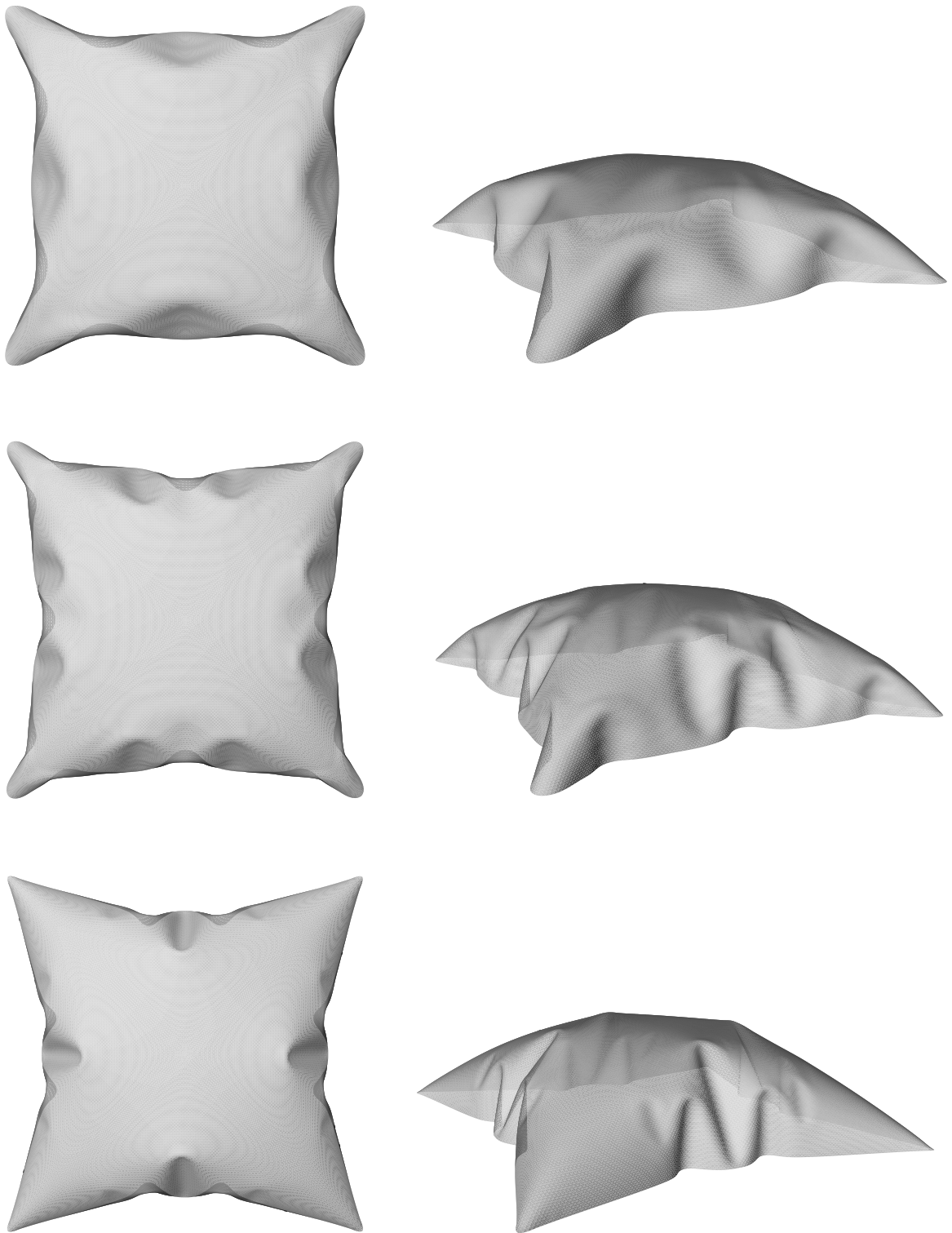   Unfortunately, the convergence properties of finite-element solutions in the nonlinear range

Figure 10: Computed quasistatic deflected shapes for the square airbag problem with a) 1635, b) 6339, and c) 24963 degrees of freedom.
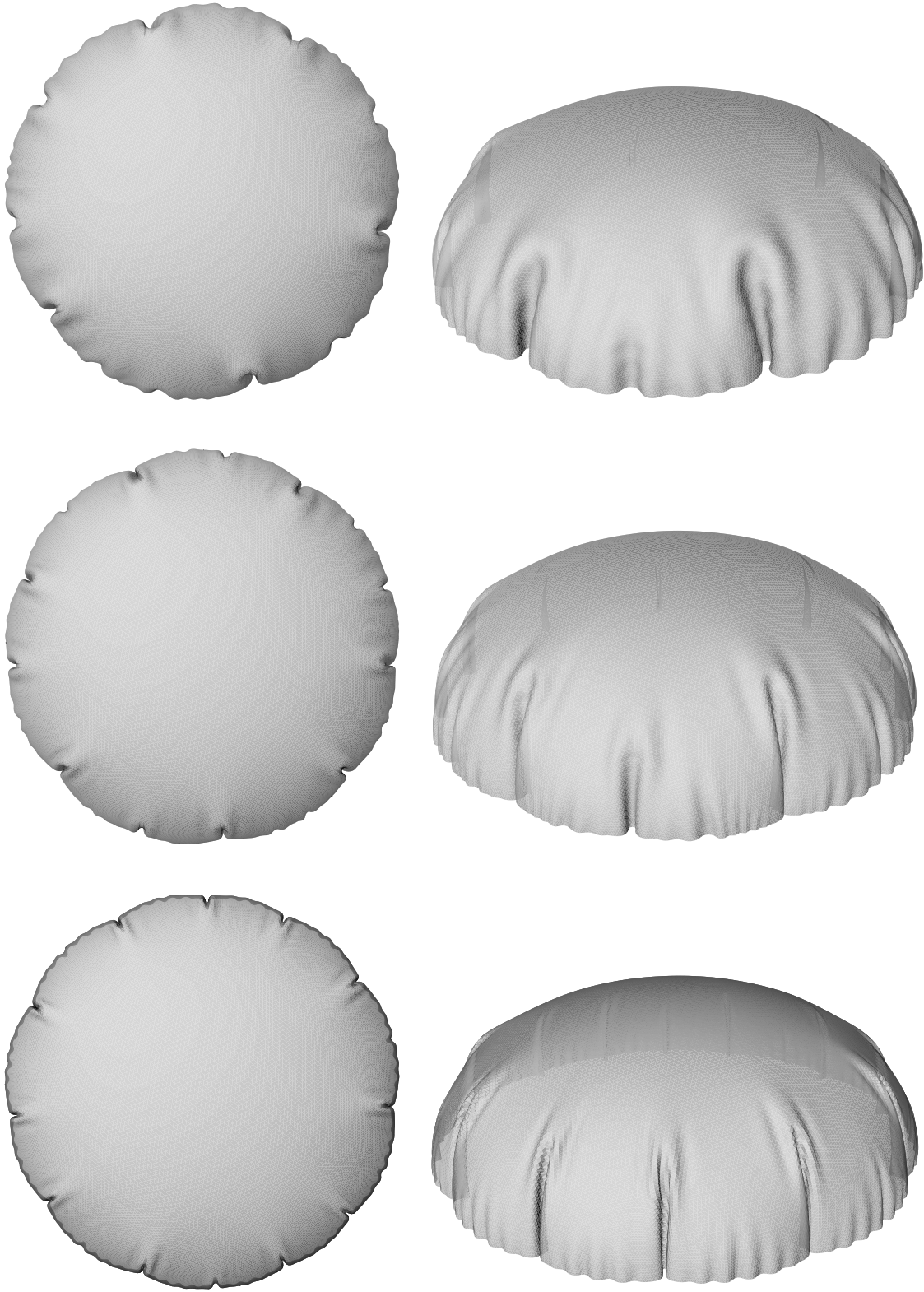
Figure 11: Computed quasistatic deflected shapes for the circular airbag problem with a) 7029, b) 27555, and c) 108867 degrees of freedom.
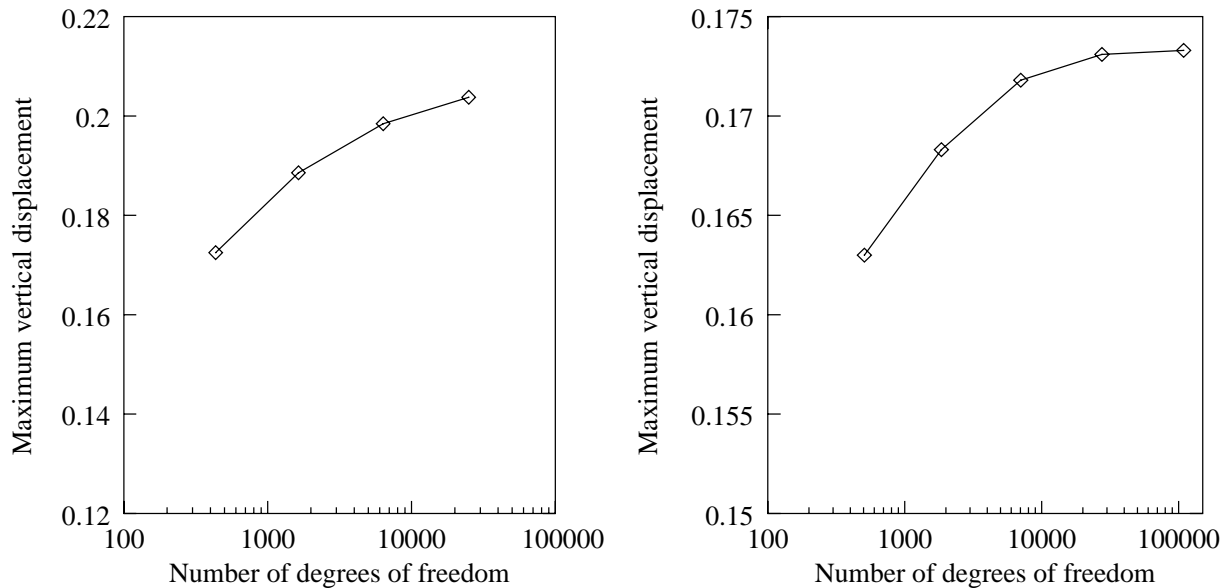
Figure 12: Convergence of maximum vertical displacement with number of degrees of freedom. a) Square airbag. b) Circular airbag.

are poorly understood at present. The chief difficulty here is the lack of convexity of the energy functional. Indeed, Ball [4] noted that convexity is incompatible with material frame indifference, fails for nearly-incompressible materials, and rules out buckling. Consequently, convexity can never be expected of the energy functional of a finitely-deforming elastic material. This lack of convexity of the energy functional results in a massive lack of uniqueness of the solution and may lead to the formation of microstructures of arbitrary fineness [5]. Under these severe conditions, the properties of finite-element solutions, or of solutions obtained by means of any other method of approximation, are fraught with uncertainty. However, for methods such as developed here, based on constrained energy minimization, energy bounds do exist in some cases [34, 33, 19, 18] which suggest convergence in energy. In the present setting, convergence in energy is simply meant to indicate that the minimum energy of the system is attainable through a process of increasing mesh refinement. The solutions to the airbag problem presented here, exhibit the intricate microstructures–in the form of fine folding patterns–which may be expected of the solutions of nonconvex problems. These intricacies notwithstanding, certain salient features of the solution, such as the maximum center deflection, do exhibit a general trend towards convergence, which attests to the robustness of the method.

Acknowledgments

References

[1] U. Andelfinger and E. Ramm. Eas-elements for two dimensional, three dimensional, plate- and shell structures and their equivalence to hr-elements. *Internat. J. Numer. Methods Engrg.*, 36:1311–1337, 1993.

[2] J.H. Argyris and D.W. Scharpf. The sheba family of shell elements for the matrix displacement method. *Aeron. J. Roy. Aeron. Soc.*, 71:873–883, 1968.

[3] D.G. Ashwell and R.H. Gallagher, editors. *Finite Elements for Thin Shells and Curved Members*, London, 1976. John Wiley & Sons.

[4] J. M. Ball. Constitutive inequalities and existence theorems in nonlinear elastostatics. In R. J. Knops, editor, *Nonlinear Analysis and Mechanics: Heriot-Watt Symposium*, volume I, pages 187–241. Pitman Publising Ltd., 1977.

[5] J.M. Ball and R.D. James. Fine phase mixtures as minimizers of energy. *Archive for Rational Mechanics and Analysis*, 100(1):13–52, 1987.

[6] Y. Basar and Y. Ding. Finite-element analysis of hyperelastic thin shells with large strains. *Comp. Mech.*, 18:200–214, 1996.

[7] K. Bell. A refined triangular plate bending finite element. *Internat. J. Numer. Methods Engrg.*, 1:101–122, 1969.

[8] T. Belytschko. An overview of semidiscretization and time integration procedures. In T. Belytschko and T. J. R. Hughes, editors, *Computational Methods for Transient Analysis*, pages 1–65. North-Holland, 1983.

[9] T. Belytschko, H. Stolarski, W.K. Liu, N. Carpenter, and J.S.J. Ong. Stress projection for membrane and shear locking in shell finite-elements. *Comput. Methods Appl. Mech. Engrg.*, 51:221–258, 1985.

[10] P. Betsch, F. Gruttmann, and E. Stein. A 4-node finite shell element for the implementation of general hyperelastic 3d-elasticity at finite strains. *Comput. Methods Appl. Mech. Engrg.*, 130:57–79, 1996.

[11] K. Bhattacharya and R.D. James. A theory of thin films of martensitic materials with applications to microactuators. *J. Mech. Phys. Solids*, 47(3):531–576, 1999.

[12] H. Biermann, A. Levin, and D. Zorin. Smooth subdivision surfaces with normal control. Courant Institute of Mathematical Sciences, New York, Preprint, 1999.

[13] M. Bischoff and E. Ramm. On the significance of higher order kinematic and static variables in a three-dimensional shell formulation. *Int. J. Solids Struct*, 1998. to appear.

[14] M.L. Bucalem and K.J. Bathe. Finite element analysis of shell structures. *Archives Comput. Methods Engrg.*, 4:3–61, 1997.

[15] N. Büchter and E. Ramm. Shell theory versus degeneration - a comparison in large rotation finite element analysis. *Internat. J. Numer. Methods Engrg.*, 34:39–59, 1992.

[16] E. Catmull and J. Clark. Recursively generated b-spline surfaces on arbitrary topological meshes. *Comput. Aided Design*, 10(6):350–355, 1978.

[17] E. Cerda, S. Chaieb, F. Melo, and L. Mahadevan. Conical dislocations in crumpling. *NATURE*, 401(6748):46–49, 1999.

[18] M. Chipot, C. Collins, and D. Kinderlehrer. Numerical-analysis of oscillations in multiple well problems. *Numer. Math.*, 70(3):259–282, 1995.

[19] M. Chipot and D. Kinderlehrer. Analysis and computation in non-convex well problems. *ZAMM*, 76(2):393–396, 1996.

[20] F. Cirak, M. Ortiz, and P. Schröder. Subdivision surfaces: A new paradigm for thin-shell finite-element analysis. *In print, Internat. J. Numer. Methods Engrg.*, 47, 2000.

[21] F. Cirak, M.J. Scott, E.K. Antonsson, M. Ortiz, , and P. Schröder. Integrated modeling, finite-element analysis, and engineering design for thin-shell structures using subdivision. *Submitted, Comput. Aided Design*, 2000.

[22] deBorst R. The zero-normal-stress condition in plane-stress and shell elastoplasticity. *Commun. Numer. Methods Engrg.*, 7:29–33, 1991.

[23] D. Doo and M. Sabin. Behaviour of recursive division surfaces near extraordinary points. *Comput. Aided Design*, 10(6):356–360, 1978.

[24] R. Eberlein, P. Wriggers, and R.L. Taylor. A fully non-linear axisymmetrical quasi-kirchhoff-type shell element for rubber-like materials. *Internat. J. Numer. Methods Engrg.*, 36:4027–4043, 1993.

[25] G. Gioia and M. Ortiz. Delamination of compressed thin films. *Advances in Applied Mechanics*, 33:119–192, 1997.

[26] F. Gruttmann and R.L. Taylor. Theory and finite element formulation of rubberlike membrane shells using principal stretches. *Internat. J. Numer. Methods Engrg.*, 35:1111–1126, 1992.

[27] E.M. Haseganu and Steigmann D.J. Analysis of partly wrinkled membranes by the method of dynamic relaxation. *Comp. Mech.*, 14:596–614, 1994.

[28] T. J. R. Hughes. *The Finite Element Method: Linear Static and Dynamic Finite Element Analysis*. Prentice-Hall, Englewood Cliffs, N.J., 1987.

[29] T.J.R Hughes and E. Carnoy. Nonlinear finite element shell formulation accounting for large membrane strains. *Comput. Methods Appl. Mech. Engrg.*, 39:69–82, 1983.

[30] T.J.R. Hughes and W.K. Liu. Nonlinear finite element analysis of shells: Part ii. two dimensional shells. *Comput. Methods Appl. Mech. Engrg.*, 27:167–182, 1981.

[31] W. Jin. *Singular perturbation and the energy of folds*. PhD thesis, New York University, September 1997.

[32] R. V. Kohn and S. Müller. Branching of Twins near an Austenite-Twinned-Martensite Interface. *Philosophical Magazine A*, A66:697–715, 1992.

[33] B. Li and M. Luskin. Finite element analysis of microstructure for the cubic to tetragonal transformation. *SIAM J. Num. Anal.*, 35(1):376–392, 1998.

[34] B. Li and M. Luskin. Nonconforming finite element approximation of crystalline microstructure. *Math. Comput.*, 67(223):917–946, 1998.

[35] C. Loop. Smooth subdivision surfaces based on triangles. Master's thesis, University of Utah, Department of Mathematics, 1987.

[36] R.H. MacNeal. Perspective on finite elements for shell analysis. *Finite Elem. Anal. Design*, 30:175–186, 1998.

[37] J.E. Marsden and T.J.R. Hughes. *Mathematical Foundations of Elasticity*. Prentice Hall, Englewood Cliffs, N.J., 1983.

[38] L. Modica. Gradient theory of phase transitions and the minimal interface criterion. *Archive for Rational Mechanics and Analysis*, 98:123–142, 1987.

[39] P.M. Naghdi. *Handbuch der Physik, Mechanics of Solids II*, volume VI a/2, chapter The theory of shells. Springer, Berlin, 1972.

[40] A. Needleman. Inflation of spherical rubber balloons. *Int. J. Solids Struct*, 13:409–421, 1977.

[41] D.R. Oakley and Knight N.F. Adaptive dynamic relaxation algorithm for nonlinear hyperelastic structures: 1. formulation. *Comput. Methods Appl. Mech. Engrg.*, 126:67–89, 1995.

[42] R.W. Ogden. *Non-Linear Elastic Deformations*. Ellis Harwood Ltd., 1984.

[43] M. Ortiz and G. Gioia. The morphology and folding patterns of buckling-driven thin-film blisters. *J. Mech. Phys. Solids*, 42(3):531–559, 1994.

[44] M. Ortiz and L. Stainier. The variational formulation of viscoplastic constitutive updates. *Comput. Methods Appl. Mech. Engrg.*, 171(3-4):419–444, 1999.

[45] A.C. Pipkin. The relaxed energy density for isotropic elastic membranes. *IMA J. Appl. Math.*, 36:85–99, 1986.

[46] G. Ramesh and C.S. Krishnamoorthy. Post-buckling analysis of structures by dynamic relaxation. *Internat. J. Numer. Methods Engrg.*, 36:1339–1364, 1993.

[47] E. Ramm. Geometrisch nichtlineare elastostatik und finite elemente. Habilitation 76-2, Institut für Baustatik der Universität Stuttgart, 1976.

[48] U. Reif. A unified approach to subdivision algorithms near extraordinary vertices. *Comput. Aided Geom. Design*, 12(2):153–174, 1995.

[49] U. Reif and P. Schröder. Curvature smoothness of subdivision surfaces. Technical Report TR-00-03, California Institute of Technology, 2000.

[50] D. Roehl and E. Ramm. Large elasto-plastic finite element analysis of solids and shells with the enhanced assumed strain concept. *Int. J. Solids Struct*, 33:3215–3237, 1996.

[51] A. Rössle, M. Bischoff, W. Wendland, and Ramm E. On the mathematical foundation of the (1,1,2)-plate model. *Int. J. Solids Struct*, 36:2143–2168, 1998.

[52] J.C. Simo and D.D. Fox. On a stress resultant geometrically exact shell model. part i: Formulation and optimal parameterization. *Comput. Methods Appl. Mech. Engrg.*, 72:267–304, 1989.

[53] J.C. Simo, D.D. Fox, and M.S. Rifai. On a stress resultant geometrically exact shell model. part ii: The linear theory; computational aspects. *Comput. Methods Appl. Mech. Engrg.*, 73:53–92, 1989.

[54] J.C. Simo, D.D. Fox, and M.S. Rifai. On a stress resultant geometrically exact shell model. part iii: Computational aspects of the nonlinear theory. *Comput. Methods Appl. Mech. Engrg.*, 79:21–70, 1990.

[55] J.C. Simo, D.D. Fox, and M.S. Rifai. On a stress resultant geometrically exact shell model. part iv: Variable thickness shells with through-the-thickness stretsching. *Comput. Methods Appl. Mech. Engrg.*, 81:91–126, 1990.

[56] J.C. Simo and J.G. Kennedy. On a stress resultant geometrically exact shell model. part v. nonlinear plasticity: Formulation and integration algorithms. *Comput. Methods Appl. Mech. Engrg.*, 96:133–171, 1992.

[57] J. Stam. Fast evaluation of catmull-clark subdivision surfaces at arbitrary parameter values. In *Computer Graphics (SIGGRAPH '98 Proceedings)*, 1998.

[58] J. Stam. Fast evaluation of loop triangular subdivision surfaces at arbitrary parameter values. In *Computer Graphics (SIGGRAPH '98 Proceedings, CD-ROM supplement)*, 1998.

[59] P. Wriggers, R Eberlein, and S. Reese. A comparison of 3-dimensional continuum and shell elements for finite plasticity. *Int. J. Solids Struct*, 33:3309–3326, 1996.

[60] O.C. Zienkiewicz and R.L. Taylor. *The Finite Element Method - Volume 2*. McGraw-Hill Book Company, Berkshire, 1989.

[61] D. Zorin and P. Schröder, editors. *Subdivision for Modeling and Animation*, Computer Graphics (SIGGRAPH '99 Course Notes), 1999.

[62] D. Zorin, P. Schröder, and W. Sweldens. Interactive multiresolution mesh editing. In *Computer Graphics (SIGGRAPH '97 Proceedings)*, 1997.